Field Monitoring and Laboratory Testing for an Integrated Modeling of River Embankments under Transient Conditions

Published Version:
Gragnano C.G., Rocchi I., Gottardi G. (2021). Field Monitoring and Laboratory Testing for an Integrated Modeling of River Embankments under Transient Conditions. JOURNAL OF GEOTECHNICAL AND GEOENVIRONMENTAL ENGINEERING, 147(9), 1-16 [10.1061/(ASCE)GT.1943-5606.0002571].

Availability:
This version is available at: https://hdl.handle.net/11585/830188 since: 2021-08-24

Published:
DOI: http://doi.org/10.1061/(ASCE)GT.1943-5606.0002571

(Article begins on next page)

Manuscript Details

Field monitoring and laboratory testing for an integrated modelling of river embankments under transient conditions

Author 1

- Carmine Gerardo Gragnano, Research fellow, PhD
- Department of Civil, Chemical, Environmental and Materials Engineering, Bologna, Italy
- 0000-0001-7767-0238

Author 2

- Irene Rocchi, Assistant Professor, PhD
- Department of Civil Engineering, Technical University of Denmark, Copenhagen, Denmark
- 0000-0003-0434-8031

Author 3

- Guido Gottardi, Professor, PhD
- Department of Civil, Chemical, Environmental and Materials Engineering, Bologna, Italy
- 0000-0003-4944-8212

Full contact details of corresponding author

Name:	Carmine Gerardo Gragnano
E-mail:	carmine.gragnano2@unibo.it
Tel:	+39 051 20 9 3521
Institution:	University of Bologna

Abstract

The need for a reliable estimate of the actual failure probability of existing river embankments under changing boundary conditions represents an ever-demanding task for researchers and designers, as well as those involved in their maintenance and management. Uncertainty and variability of soil suction and water content spatial and temporal distributions, together with the definition of a suitable soil model that takes into account the partially saturated state of embankment materials, are among the most critical aspects to be possibly included in the advanced analysis and design of such linear earthen infrastructures. The use of specialist integrated monitoring can be here functional to enable calibration and to enhance reliability and consistency of predictive analyses. Site measurements of main variables at relevant depths are typically rarely available, while an accurate soil characterization under partially saturated conditions is only performed in research applications, thus producing limited confidence on stability conditions. In order to provide a useful and innovative tool to evaluate realistic stability conditions of levees under transient flow conditions, a full-scale monitoring system has been implemented on an existing section of the river Secchia (Northern Italy) 11 m-high flood defences. The complementary use of specific laboratory tests, innovative field measurements and numerical analyses presented in the paper aims at providing a suitable methodological approach to the performance assessment of these vital geotechnical systems throughout their entire lifetime and highlighting possible limitations of typically used methods of analysis.

Keywords
river embankments, transient seepage, field monitoring, partial saturation, suction.

List of notations

A	is the inverse of the relative humidity at the soil surface
c'	is the effective cohesion
c_c	is the coefficient of gradation or curvature
c_u	is the coefficient of uniformity
D_{10}	is the diameter corresponding to 10% finer in the grain size distribution
D_{50}	is the diameter corresponding to 50% finer in the grain size distribution
D_v	is the vapour diffusion coefficient
E	is the net radiant energy available at the surface
E_a	is an evaporative parameter function of wind speed and surface roughness

g	is the gravity acceleration
G_s	is the specific gravity
I_{cn}	is the soil behaviour type index, defined as $((3.47 - LogQ_t)^2 + (1.22 + LogF_r)^2)^{1/2}$
I_P	is the index of plasticity
k	is the soil permeability
k_r	is the relative permeability
k_{sat}	is the saturated soil permeability
k_x	is the soil permeability in x direction
k_z	is the soil permeability in z direction
m_{VG}	is a model parameter for the retention curve
m_w	is the water storage coefficient
n_{VG}	is a model parameter for the retention curve
p_v	is the soil moisture vapour pressure
q_t	is the cone resistance corrected for pore water effects, defined as $q_c - u_2(1 - a)$ where a is the cone factor
Q	is the applied boundary flux
RH	is the relative humidity
S_e	is the effective degree of saturation
SF	is the safety factor
T	is the temperature
t	is the time
u_a	is the pore pressure of the air phase
u_p	is the psychrometric constant
u_w	is the pore pressure of the water phase
u_0	is the pore pressure having hydrostatic profile
u_2	is the penetration pore pressure immediately behind the cone tip
w_{LL}	is the water content at liquid limit

z	is the elevation head or depth below ground level
α_{VG}	is a model parameter for the retention curve
β_d	is the reliability index
γ_{sat}	is the saturated unit weight of soil
Γ	is the slope of the saturation vapour pressure versus temperature curve at the mean air temperature
φ'	is the effective angle of shearing resistance
λ	is the heat specific capacity
θ	is the volumetric soil water content at the actual state
θ_r	is the volumetric soil water content at the residual conditions
θ_{sat}	is the volumetric soil water content at saturation
ρ_w	is the water density
σ_n	is the total normal stress
σ_v	is the total vertical stress in situ
σ'_v	is the effective vertical stress in situ
τ	is the soil shearing resistance stress
AE	is the Actual Evaporative flux
CPTU	is the Cone Penetration Test including pore-water pressure measurements (piezocone)
FF	is the Fines Fraction
MP	is a Multi-Point borehole installation
SP	is a Single Point borehole installation
SWRC	is the Soil Water Retention Curve

1. Introduction

River flooding subsequent to sudden collapse of water-retaining infrastructures is a worldwide recurrent phenomenon. Over the last few decades, a rising number of devastating events has been experienced globally. Numerous studies on the socio-economic impact of floods have indicated an increase in people and assets exposed to this threat, mainly due to a combination of erroneous or missing land-use planning and to the overall increase of weather-related natural disasters (Tanoue et al., 2016). Climatic and hydrological changes, from regional to global scale, affect the hydraulic and retention performance of existing earthen water-retaining structures and may increase the frequency or magnitude of flooding, establishing novel and potentially critical conditions (Toll et al., 2012). Stability analysis of river embankments thus represents a crucial step in the framework of environmental risk assessment and management. For this type of linear earthen infrastructures, strength arising from partially saturated conditions represents a fundamental source of resistance towards global slope instability (Casagli et al., 1999; Gottardi and Gragnano, 2016; Toll et al., 2016), which may be described by an apparent cohesion term (e.g. Fredlund et al., 1978) and depends primarily on soil suction and water content values. However, typical stability analyses do not often consider these two quantities, as they are strongly affected by experimental uncertainties, time and spatial variability (Gottardi et al., 2020) and, more generally, their determination is subordinate to cost-related issues. Furthermore, a rather limited number of direct and continuous site measurements is currently available to provide a reliable benchmark and thus numerical models able to reproduce the embankments partial saturation state cannot be suitably calibrated and validated. Among these, Rivera-Hernandez et al. (2019) recently demonstrated how to use effectively field-monitoring data to improve the numerical simulation of a levee under climatic and tidal variations. The case study showed the use of field monitoring to calibrate and validate saturated-unsaturated transient flow analyses to predict pore-water pressures more accurately under various climatic loads.

The determination of actual water flow through the filling material is a main concern for the stability assessment of levees and, in general, of earthen-structures performance (Ridley et al. 2004; Rinaldi et al. 2004; Calabresi et al. 2013; Pozzato et al. 2014; Stark et al., 2017). A common approach to this problem is the use of Finite Element Method (FEM) numerical modelling associated with stability analyses carried out by either Limit Equilibrium Methods (LEM) or Strength Reduction Methods (SRM). Several comparisons between LEM and SRM results point to a good agreement in terms of critical slip surface locations, but overall find slightly lower Safety Factors for LEM (Griffiths & Lane., 1999; Duncan 2000; Liu et al., 2015; Mouyeaux et al. 2018). Alternatively, advanced numerical modelling of flow in porous media should account for a fully-coupled hydromechanical analysis. This has been extended to the case of unsaturated earthen structures under extreme precipitation and flood events by Jasmin et al. (2017) and Vahedifard et al. (2018), among others.

The present study focuses on the safety assessment of river embankments towards global instability by means of LEMs, considering as key aspects the suction and water content variations caused by significant hydrometric fluctuations (more than 10m). A methodology is established to perform FEMs transient seepage analyses, where a comprehensive experimental dataset combining field and laboratory results provide the relevant input for numerical modelling, requiring calibration of only one parameter in order to match field observations. Furthermore, the study demonstrates the effects of recent hydrometric time-history on the factor of safety and the result of using as initial condition the pore-water pressure distribution as measured in situ, rather than the conventional hydrostatic distribution. The case of a major flood embankment along the river Secchia, a South affluent of the river Po (Northern Italy), has been here considered as a study case.

A major flooding event occurred in January 2014 at an upstream section of the same river Secchia after sudden embankment collapse (D'Alpaos et al., 2014). The decrease in suction values of the filling material due to a series of consecutive high-water events and contemporary heavy rainfalls are likely to have favoured a global instability mechanism, which was probably facilitated by local weakening due to the widespread presence of animal burrows (Orlandini et al., 2015). Eventually, river-water overtopping quickly induced a 20 m-long breach in the earthen structure, which was about 5.5 m-high above the ground level. The subsequent flooding event involved approximately 38 million cubic meters of water, causing one casualty and long-lasting damages to a vast surrounding area (Figure 1). In total, approximately 200 million euros were allocated to restore public structures, private properties and levees. This rather unexpected catastrophic event raised several questions on the actual margin of safety of the entire flood embankment system of the river Secchia, in particular, and of other adjacent rivers having similar characteristics.

The outcomes and findings discussed in this paper are reckoned to address some of the questions raised about the overall stability of river embankment systems typically encountered in the study area, as a result of changes in climate. Furthermore, the methodology employed is generally valid in providing researchers and practitioners with novel useful indications to be taken in due consideration when analysing the time-variable stability conditions of linear earthen infrastructures, such as river embankments.

2. Geotechnical model of the experimental site

2.1 Study area

An embankment section of river Secchia, about 15 km downstream the breach occurred on January 19th 2014, was selected for carrying out an extensive experimental study. The area (Figure 2) was chosen because of easy-access to the crest and to the banks, nearby pre-existing standard geotechnical in-situ tests (including CPTU) and monitoring devices (including piezometers), and frequent flooding of the riverbank due to limited berm width. The instrumented embankment section is approximately 11 m-high from the ground level, i.e. about 33 m above the mean sea level. The crest is 4.6 m wide, hosting a light traffic road, while a naturally produced berm toward the river side, located about 5.2 m below the crest, is about 5.5 m wide (Figure 3a). Slope angles toward the river and landward are about 30° and 25°, respectively, typically kept free from high vegetation with periodic mowing (twice a year).

2.2 Stratigraphic model

The stratigraphic model was formulated based on several boreholes performed in connection with sensor installations and following the execution of four CPTU tests, extended to greater depth, whose position is sketched in Figure 2, while their profiles are presented in Figure 3(b). In particular, two tests were performed from the embankment crest (CPTU1 and CPTU2) and two from its berm (CPTU3 and CPTU4), in order to investigate two adjacent cross sections of the levee (see Figure 2). As observed in Figure 3(b), the depth investigated was significant (between 15 and 25m), due to the considerable height of the embankment.

Based on q_t, the cone resistance corrected for pore water effects as measured immediately behind the cone tip u_2, the sleeve friction f_s and the hydrostatic pore pressure u_0 as provided by piezometers, the soil behaviour type index I_{cn} was calculated in order to make use of Robertson's chart (Robertson, 2009). Note that there is nearly no pore-water pressure recorded above the water table, which was at around 9 m below the crest elevation based on piezometric measurements at the time of testing. This is because of highly unsaturated conditions in the embankment during summer, when tests were performed, due to the low river water level as indicated in Figure 3(a). Therefore, the cone resistance should be used with care in standard correlations, as suction is likely to affect relevant measurements (Yang & Russel, 2016). To partly account for the effects of suction, the effective stress used for normalisation of cone resistance was calculated based on the negative pore-water pressure profile typical of summer, as obtained from monitoring. Furthermore, the soil classification was closely compared to geological descriptions of the borehole cores to validate the results.

The I_{cn} trend with depth is shown in Figure 3(a), where only the profiles obtained from CPTU1 and CPTU4 are reported, as they are the closest to the monitoring section. The grid on the x-axes divides I_{cn} values representative of different soil behaviour type (e.g. sand or silt), where lower values indicate coarser material. Despite the stress level correction introduced for data normalisation, I_{cn} values at shallow depths are not fully in agreement with particle size distributions presented in Table 1. Within the first 2 m suction can reach extremely high values, as it will be shown in the following, and therefore greater discrepancy from the borehole logs was found at shallow depths because of the high values of q_t measured, likely linked to overconsolidation by desiccation besides high suction. Information reported in Table 1 will be further discussed later in the paper.

The I_{cn} trend with depth shows thin interbedding and a mix of fine to coarse graded soils for a given unit, providing a rather heterogeneous soil profile. However, the degree of heterogeneity is similar for the two cross sections investigated, suggesting that the monitoring results can be regarded as representative of the whole investigated area. Despite the heterogeneity observed, a relatively small number of distinct soil units could be identified (Figure 3a). Unit A includes the embankment deposits that can be ascribed to natural and anthropic origin and consist of an alternation of silts and sandy silts. In particular, this unit was subdivided in Unit A and Unit A' due to a general coarsening trend towards the river, as a result of fluvial sediments deposition during past flooding events. At about 26 m above the mean sea level, there is a relatively sharp change from interbedded silts and sandy silts to silts and silty clays, which determines the transition from Unit A to Unit B. At about 16 m elevation, a 1-2 m thick layer having slightly coarser grading is found (Unit C), which appears to have good permeability and continuity over the area, as it rapidly responds to any change in the adjacent river water level – based on the relevant piezometric measurements discussed later on. Underneath Unit C, a rather uniform clay layer (Unit D) was found to the maximum investigated depth.

2.3 Soil characterisation

Extensive laboratory investigations were performed for determining physical, hydraulic and mechanical properties of soils, including standard and advanced tests (Gragnano et al., 2018; Gragnano et al., 2019). In particular, the river embankment material (Unit A) was investigated in detail, as it represents the main volume of interest for the studied section and it hosts most of the monitoring sensors. The top of the levee has a 0.5 m-thick layer of compacted coarse-grained soil, which has been placed as foundation for a light traffic road on the crest of the embankment. Below this layer, embankment filling material was identified and its physical properties are summarised in Table 1. Classification tests performed on the clay fraction (ranging between 10 and 25% in Unit A) exhibit low plasticity, with plasticity index (I_p) of about 10-13% (Rocchi et al., 2018a). These values suggest that tension cracks and fissures at shallow depths are unlikely to form and, in fact, these have never been observed at the ground surface of the considered embankment sector, even during summer drying.

Figures 4 (a-d) show the Soil Water Retention Curves (SWRC) representative of the soil behaviour in partially saturated conditions, as determined in the laboratory on soil sampled up to 6.9 m depth. The curves show the interpretation of the experimental data obtained along main drying branches according to the van Genuchten model (van Genuchten, 1980), where continuous and dashed lines represent intact and reconstituted specimens, respectively. In the same figure, the SWRCs traced by coupled sensors in the field along drying (a and b) and wetting (c and d) branches are also shown by symbols, as discussed later. Extensive laboratory measurements were performed on samples having initial void ratios e_0 varying in the range 0.48 – 0.86, as reported in the figures. A combination of the evaporation method, from high to intermediate values of saturation (Schindler et al., 2012), and of the chilled mirror method, towards the dry region of the SWRC (Kriste et al., 2019) has been used to determine main drying curves. Extended evaporation methods were also used for additional information on intermediate to low values of saturation (Schindler et al., 2010; Schelle et al., 2013). The water flow during the experiments is measured from the evaporation loss through the soil free surface and by combining it to the hydraulic gradient based on the suction measurements in the soil sample, the hydraulic conductivity can be estimated by inversion of the Darcy's law (Peters & Durner, 2008). For samples taken from the embankment crest (Figures 4a and 4c), the soil was tested both in its undisturbed and reconstituted state, as undisturbed soil sampling of such dense silty-sandy soils turned out to be quite difficult, while only undisturbed soil samples were tested for Units A' and B (Figure 4b and 4d). Several tests were performed on Unit A and Unit A', that plot in a well-defined area despite the relative heterogeneity. The reconstituted samples (dashed lines), which were prepared by compaction at a void ratio similar to that measured on undisturbed samples, tend to show slightly higher air entry value and flatter curves than the intact samples (continuous lines). Laboratory measurements on undisturbed samples appear to be close, but generally above the field observations, as could be expected for the hysteretic response of wetting-drying cycles in situ. The average soil retention parameters derived from laboratory tests on those units in partially saturated conditions are listed in Table 2 (Unit A, A', B and E). These parameters, which were used as input for the numerical modelling discussed later, provide the relationship between the soil suction, expressed as the difference between pore pressure of the air and the water phases ($u=u_a-u_w$), and the dimensionless water content or the equivalent effective degree of saturation, S_e, as according to the widely-adopted van Genuchten model (van Genuchten, 1980):

$$1.\ S_e = \frac{\theta-\theta_r}{\theta_{sat}-\theta_r} = \left\{\frac{1}{1+[(u_a-u_w)/\alpha_{VG}]^{n_{VG}}}\right\}^{1-\frac{1}{n_{VG}}}$$

where θ, θ_{sat} and θ_r are the volumetric soil water content at the actual state, at saturation and at residual conditions respectively, u_a and u_w are the pore pressure of the air and water phases respectively, while α_{VG} and n_{VG} are model parameters, mainly influencing the inflection and the shape of the retention curve in a semi-logarithmic plane.

The saturated permeability k_{sat} was as a first attempt inferred through interpretation of relevant site tests (Robertson & Cabal, 2012) in order to obtain statistically representative values. Due to partial saturation within the embankment, however, this parameter was further estimated from evaporation test results for Unit A and Unit A', following the method outlined by Peters & Durner (2008). For example, the value obtained for Unit A was on average equal to $9.5\text{x}10^{-08}$ m/s, and $2.9\text{x}10^{-07}$ m/s for site and laboratory test results, respectively. Given the discrepancy, the significant degree of uncertainty related to k_{sat} experimental determination and intrinsic variability of this parameter, a sensitivity analysis of the transient seepage analysis results was performed. Eventually, this parameter was calibrated to be equal to $6.2\text{x}10^{-07}$ m/s (as reported in Table 2). Furthermore, Table 2 shows the values of effective angles of shear strength as obtained from CPTU1 and CPTU4 data interpretation. Note that for Unit E the mechanical parameters have been assumed equal to those of Unit B, due to lack of data, while k_{sat} was obtained from a single laboratory test (dash dot line in Figures 4 a and c).

Similarly to what performed for the soil classification, the actual effective stress was calculated based on the measured negative pore pressure profile, in order to minimize the influence of suction on the soil shear strength determination. These results should be however treated with caution as the used correlations were developed for saturated soils (Kulhawy & Mayne, 1990; Mayne & Campanella, 2005, for coarse- and fine-grained layers, respectively). Shear strength parameters in Units A and B (solid lines in Figure 5) exhibit a nearly normal distribution (dashed lines), as obtained from the estimated values of average (30.6° and 24.9°, respectively) and standard deviation (1.1° and 0.6°, respectively) determined from the interpretation of CPTU1 test results.

3. Monitoring system

The monitoring system, designed and gradually installed over a time period of 18 months, is based on the outcome of the geotechnical investigation above described and of preliminary numerical analyses on this specific levee section (Rocchi et al., 2018b) and a similar one (Gottardi et. al, 2016). It includes twenty sensors that were installed and positioned as described in this section. Various devices exist for measuring soil suction or hydraulic potential and water content in situ, mostly operating through indirect techniques (Tarantino & Pozzato, 2008; Bittelli, 2011). However, installation at considerable depth poses several constraints on the sensor choice. In particular, because the embankment has been already in operation for several decades, it was not possible to embed the sensor during its construction and at the same time it was crucial to limit the impact of the monitoring system installation on the infrastructure. Finally, the idea was to implement a relatively low cost and low maintenance system to increase the potential for similar solutions to be applied in engineering practice.

To minimize the number of boreholes drilled, most were equipped with multiple sensors. In addition, water content and suction sensors were positioned at a short distance within a single borehole to couple their measurement and obtain a soil water retention curve in situ. These boreholes are identified in Figure 6 as Multi-Point (MP), whereas sensors having a dedicated installation borehole are identified as Single Point (SP). Furthermore, the sensor ID specifies the location of installation by either B or C, which stand for Berm and Crest/Crown, respectively. A sequential number corresponding to the installation order follows. The majority of the installations provides an indirect measurement of water potential and therefore tensiometers (identified as T in Figure 6) were also installed on dedicated boreholes to validate the results. Furthermore, the reliability of multi-points was assessed by repeating similar installations with a single sensor per borehole. As seen in Figure 6, four different types of commercially available sensors were used, two for measuring water content (GS3 and SM150T) and two for pore-water pressure (T8 and MPS-6). These sensors have been developed and so far routinely used for agricultural purposes, but their application to geotechnical problems, which has only recently started, is constantly increasing (e.g. Smethurst et al. 2006; Nguyen et al. 2010; Harris et al. 2013; Cascini et al. 2014).

The GS3 works correlating the dielectric permittivity of a 160cm^3 cylindrical soil volume to its water content, as this is the volume investigated by a 70 MHz electromagnetic field generated along the 6.5 mm long metal rods of the sensor. Its nominal default accuracy is ±3% (Decagon Devices, 2016a). A user calibration on representative volumes of recompacted soil sampled in situ was performed in laboratory conditions on the GS3 sensors, prior to their installation, to improve manufacturer's accuracy. The SM150T uses the same working principle, but it has two rods only and uses a 100 MHz frequency with soil moisture measurements accurate to ±3% (Delta-T Device, 2016). For these instruments, a default calibration based on soil lithotype was used for interpreting monitored raw data.

The T8 is a tensiometer working in the range -85 to +100 kPa, with ±0.5 kPa nominal accuracy (UMS, 2011). Since the pressure sensor is separated from the soil by a ceramic cup, this requires refilling in case of desaturation, which can be easily achieved from the ground surface through a thin metallic tube housed in the tube that contains the sensor cable. The MPS-6 measures the dielectric permittivity of a porous ceramic disc and provides the hydraulic potential based on its water retention curve. Unlike the tensiometer, it can only measure negative values of pore-water pressure (i.e. suction) and works over a range from -9 to -10,000 kPa with nominal accuracy ± (2 kPa + 10% of the reading) in the range -9 to -100kPa (Decagon Devices, 2016b). Main details of the installed probes (borehole ID, sensor type, installation depth, type of measurement) are listed in Table 3. More specific details regarding the user-calibration of the sensors and their performance are provided in Rocchi et al. (2020).

Regarding installation, innovative techniques - described in greater detail in Rocchi et al. (2018a) - were purposely developed in order to allow the installation of up to four sensors inside the same borehole and achieve reliable measurements in the undisturbed surrounding soil. A sketch of the coupled installation is provided in Figure 7(a), where a GS3 sensor is installed deeper than an MPS-6 sensor.

The MPS-6 water potential sensors were embedded in a cylindrical soil sample pre-compacted at target water content and density (Figure 7b), corresponding to the values at the installation depths, leaving a slot for other sensor cables to run through the sample and hence avoiding any damage during installation. The GS3 sensors instead were installed directly in the undisturbed soil surrounding the borehole using a Quick Borehole Installation Tool (Q-BIT). The Q-BIT can be operated from the ground surface using a handle that controls a set of lever mechanisms to push the metallic rods of the sensor through the lateral wall of the borehole. A detail of the tool hosting the sensor can be observed in Figure 7(c). Considerable force can be applied, as the tool rests on the opposite side of the borehole wall while thrusting the probe in place. A set of manually operated rods were used instead for deeper installations or to install SM150T sensors, but only vertically into the base of the borehole.

Therefore, water content sensors GS3 and SM150T time-response is immediate, as highlighted by the results collected since the beginning of the monitoring campaign, exactly because they are inserted directly in the natural soil. Regarding pore-water pressure measurements, because hydraulic contact is ensured between the soil and the ceramic tip of T8 tensiometers, their time response depends on the matric potential of the surrounding soil and the porous block, varying from minutes to a few hours. For these sensors, the borehole was not backfilled, as the tensiometer can be extracted and potentially reused. The borehole was therefore cased laterally with a plastic tube and its head was sealed. The MPS-6 sensors could not be inserted directly in the undisturbed soil surrounding the borehole, which results in a slight delay in their response. However, this is negligible as long as the permeability of the intact and recompacted soil is not significantly different. To ensure continuity between the sensor and borehole surroundings, (which improves the time-response of the water content sensors and MPS-6s), the boreholes were backfilled with recompacted natural soil in proximity of the sensor depth. Hydrated bentonite pellets were used in the adjacent half meter above the installation to guarantee a hydraulic seal along the sensors cable**.** The remaining of the borehole was also backfilled with natural soil, except for a bentonite seal in proximity of the ground surface.

4. Monitoring data

Figure 8(a) shows the monitored data potentially sensitive to river level fluctuations regarding pore-water pressure, where negative values represent suction, for a 5-months period between December 1st 2017 and April 30th 2018, comprising one full winter period. The corresponding hydraulic water level in m a.s.l. is also shown as reference, where specific time instants that have been used for subsequent numerical analyses are highlighted with circles. All observed variations of pore-water pressure remain within the range -20 to +80 kPa in Figure 8(a).

Two significant high-water events occurred during the period considered. The first had a maximum river level equal to 30.9 m (13/12/2017 04:00) and persistence of water above the berm (i.e. the period when the water level was higher than 28.1 m) of about 139 hours (from 11/12/2017 17:30 to 17/12/2017 12:00). This event is thus critical in terms of maximum water height, but low in persistence. The second high-water event had a maximum river level equal to 30.1 m (13/03/2018 09:00) and persistence of water above the berm of about 343 hours (from 08/03/2018 03:00 to 22/03/2018 10:00), thus having a lower maximum water level, but greater persistence with respect to the first event. The peak water levels for the two events are about 3 months apart. Therefore, their effects are not concurrent, even though the actual hydrometric time-history is reflected in a different pore-water pressure distribution in the levee at the beginning of each event.

With regards to the instruments installed from the crest of the embankment (identified by C in Figure 8), they appear to be linked to river water levels as long as these are persistent. At significant depth, but still within Unit A (TC2, SPC1 and MPC3), the measured values change only slightly during the observation period. However, there are two time intervals where a clear response can be noticed, occurring while the water level in the river is already lowering. In particular, following the first high-water event in December 2017, measurements from TC2 register a variation from -13 kPa (05/01/2018 00:00) to about -6 kPa, reaching a stable value starting from the beginning of February (06/02/2018 16:00). In response to the second event, a maximum value of about +7 kPa (22/03/2018 01:00) is measured in TC2, followed by a smooth reduction in pore-water pressure with time. Thus, a maximum excursion of about 20 kPa in pore-water pressure is experienced at 8.0 m depth, corresponding to nearly 2 m rise in the water table (i.e. saturation level) within the levee. These data are confirmed by MPS-6 measurements in SPC1 (7.0 m depth) and MPC3 (6.2 m depth). Following the high-water event in

March 2018 on 15/03/2018 and 27/03/2018, respectively, these sensors reached the upper limit of -9 kPa, resulting in an increase of about 12 kPa since their respective values in early December 2017. It is worth noticing that suction data measured in MPC3, SPC1 and TC2 tend to reduce with comparable trends following the two high-water events in December 2017 and March 2018, which confirms that the time response of MPS-6 is acceptable when compared to T8 within a valid measuring range.

Figure 8(b) shows the pore-water pressure monitored data potentially sensitive to precipitations, as well as river level fluctuations, for the same period as in Figure 8 (a). Concerning the instruments located inside the river berm at shallow depth (marked with void symbols and labelled by B for berm, i.e. MPB1, MPB2 and SPB1), initially their values are between -20 kPa (MPB2) and -1 MPa (MPB1). As a result of the first high-water event there is a sharp reduction in suction that goes beyond the sensor measuring range (i.e. -9 kPa). For this reason, the axis is cut at -10kPa, as readings above are not reliable for MPS-6 sensors (dashed lines in Figure 8). MPC2 at depth 1.2 m from the crest, which initially records -2 MPa, instead sees a reduction in suction only in February 2018, as precipitations intensify. The reduction in this case is smoother and eventually this sensor also exceeds the measuring range. The values of suction measured by MPC1 (3.1 m and 4.6 m depth) tend to remain quite constant throughout the monitored period, suggesting a limited influence of both precipitations and river level variations at these depths. The tensiometer TC1, which is installed at approximately the same depth as the deeper sensor in MPC1, provides a comparable value at the start of the observation time that remains quite constant until the beginning of March 2018. Note that the occasional sudden changes in pore-water pressure (shown in grey in Figure 8(b)) are due to water infiltration in the protection tube from surface.

For the sake of brevity, the time series relative to water content measurements are not reported here (see Rocchi et al., 2020), but the SWRCs traced by all coupled sensors are anyway shown in Figure 4. In particular, drying branches measured at various depths from the crest and the berm of the embankment are plotted respectively in Figure 4(a) and Figure 4(b); analogously wetting branches are plotted in Figure 4(c) and Figure 4(d). Due to the fact that a rapid response is measured by shallow sensors in wetting (during intense rainfall and high-water events), the corresponding hydraulic paths may not be fully representative of the real soil retention behaviour as the response of suction and water content probes is not simultaneous. For this reason, only initial and final coupled data for these sensors should be considered as reliable for soil characterisation. Difference in the variation of values can again be observed when comparing deep and shallow measurements where greater excursions in suction and water content values are observed for shallow sensors. In order to investigate the soil water retention behaviour in situ within a wider range, it can be therefore beneficial to monitor the shallow (above 1.5 m depth) zone of the embankment.

5. Numerical modelling of the hydraulic and retention soil behaviour of the river embankment

5.1 Governing equations and boundary conditions

The time period considered for transient flow analyses, consistently with the monitoring data presented in the previous section, goes from December 1st 2017 to April 30th 2018. Modelling the atmospheric coupling in a seepage analysis represents the main theoretical and practical tool for the determination of time-dependent pore-water pressure (including suction) and water content distributions in the domain of analysis, i.e. the monitored levee section. Therefore, the numerical FE software VADOSE/W (Geo-Slope International Ltd, 2012) was used to determine water flow patterns through the river embankment under the effect of variable hydrometric and climatic conditions. The governing differential equation for the 2D hydro-thermal seepage and heat transfer implemented in the numerical code can be expressed, respectively, as:

$$2.\ \frac{1}{\rho_w}\frac{\partial}{\partial x}\left(D_v\frac{\partial p_v}{\partial x}\right)+\frac{1}{\rho_w}\frac{\partial}{\partial z}\left(D_v\frac{\partial p_v}{\partial z}\right)+\frac{\partial}{\partial x}\left(k_x\frac{\partial\left(\frac{u_w}{\rho_w g}+z\right)}{\partial x}\right)+\frac{\partial}{\partial z}\left(k_z\frac{\partial\left(\frac{u_w}{\rho_w g}+z\right)}{\partial z}\right)+Q=m_w\frac{\partial u_w}{\partial t}$$

$$3.\ L_v\frac{\partial}{\partial x}\left(D_v\frac{\partial p_v}{\partial x}\right)+L_v\frac{\partial}{\partial z}\left(D_v\frac{\partial p_v}{\partial z}\right)+\frac{\partial}{\partial x}\left(k_{t,x}\frac{\partial T}{\partial x}\right)+\frac{\partial}{\partial z}\left(k_{t,z}\frac{\partial T}{\partial z}\right)+Q_t+\rho_c\left(V_x\frac{\partial T}{\partial x}+V_z\frac{\partial T}{\partial z}\right)=\lambda\frac{\partial T}{\partial t}$$

Where u_w = pore-water pressure in the soil, p_v = soil moisture vapour pressure, k_x and k_z = soil permeability in x and z directions, Q = applied boundary flux of water, m_w = water storage coefficient equal to the slope of the SWRC, D_v = vapour diffusion coefficient (Wilson 1990), z = elevation head, ρ_w = water density, g = gravity acceleration, λ = heat specific capacity, t = time, L_v = latent heat of vaporization, $k_{t,x}$ and $k_{t,z}$ = thermal conductivity in the x and z directions and ρ_c = volumetric specific heat value. It has to be noticed that the coefficient of water volume change, m_w, approaches the value of the coefficient of volume change, m_v, as the soil becomes saturated; this latter, for all soil layers in the present application, has been however always set to zero. Thermal conductivity and volumetric heat capacity of soil have been estimated according to Johansen et al. (1975) and Johnston et al. (1981), respectively, due to lack of more specific information. Any freezing process and its consequences from both hydraulic and mechanical points of view have been neglected in the analysis. The variation of soil permeability with suction was derived from the SWRC according to Mualem's model (Mualem, 1976), with parameters suggested by van Genuchten (1980) and described in the following equation:

4. $\mathrm{k} = \mathrm{k_{sat}}\,\mathrm{k_r} = \mathrm{k_{sat}}\,\mathrm{S_e}^{0.5}\left[1-\left(1-\mathrm{S_e}^{\frac{1}{\mathrm{m_{VG}}}}\right)^{\mathrm{m_{VG}}}\right]^2$

where the relative permeability, k_r, is determined from the effective degree of saturation, S_e.

The numerical model was built based on the geometrical data already described and the geotechnical parameters, determined as explained in the previous sections, were used as input. Note that average values were used and the only calibrated parameter was the saturated permeability of levee as already explained (Table 2). An adaptive time stepping, ranging from 1800 to 43200 seconds, has been considered for transient analyses. Assuming 0.40 m as approximate global element size for the unstructured mesh, as determined from a preliminary mesh sensitivity analysis, a total number of 9530 nodes, 9319 elements, both triangular (6-noded) and quadrilateral (8-noded) with three and four integration points respectively, were generated for the seepage analysis. Furthermore, a series of three surface layers have been defined at ground level having a 0.30 m thickness, thus avoiding numerical instabilities that may have been particularly critical with reference to elements located near the ground surface; in the present application, all surface layers share the same properties with the underneath soil layer. The calculation mesh is sketched in Figure 9, together with the definition of soil units and boundary conditions.

The key for a suitable modelling of the vadose zone is here related to the possibility of predicting the ground surface boundary conditions by using commonly available atmospheric input data (e.g. maximum and minimum values of daily temperature and relative humidity, rainfall and wind speed), being the magnitude of surface infiltration and actual evaporation the variables to be quantified. Atmospheric coupling is achieved by firstly calculating the soil Actual Evaporative flux (AE) as follows:

5. AE = $\frac{\Gamma \mathrm{E}+\upsilon \mathrm{E_a}}{\upsilon \mathrm{A}+\Gamma}$

where Γ = slope of the saturation vapour pressure versus temperature curve at the mean air temperature, E = net radiant energy available at the surface, E_a = evaporative parameter dependent on wind speed and surface roughness defined by the Modified Penman Approach (Wilson, 1990),

υ_p = psychrometric constant and A = inverse of the relative humidity at the soil surface. In case of surface infiltration, the model also allows for runoff calculation and water to pond, building up a positive pressure head in any low point along the surface. In case the precipitation rate is higher than the actual evaporation, infiltration flux is then applied as a boundary condition. If the nodal flux is less than the original amount (i.e. rainfall), then runoff is calculated as:

6. Runoff = Precipitation – AE – Infiltration.

Such formulations extend the conventional Penman method (Penman, 1948) to unsaturated conditions, while computing evaporation from the soil surface and accounting for net radiation, wind speed, and relative humidity as boundary conditions. The relative humidity of the soil surface is thus evaluated by simultaneously solving the rigorously coupled moisture and heat flow equations, also considering the vapour flow component.

The input data for the atmospheric boundaries, assigned to all surface nodes, were expressed in terms of maximum and minimum daily temperature, relative humidity, rainfall intensity and wind speed, all measured within 10 km from the experimental site from a single weather station (being the closest available) and plotted in Figure 8(c) for the time period from December 1st 2017 to April 30th 2018. Transpiration by plants was not considered in the presented analysis, since the embankment is periodically mowed and the vegetation effect arising from grass is not significant here for modelling the levee stability under transient seepage conditions. The road at the top of the embankment can host light traffic and is made of compacted sand and gravel for a layer of about 0.50 m. Because these are permeable materials, the atmospheric interaction processes as well as the stability of the embankment are not significantly affected by the road presence. Homogeneous atmospheric conditions were therefore applied to the model.

On the river side, the hydrometric water level fluctuations measured in correspondence of the monitored section were imposed to external nodes as time-variable hydraulic head. Landward, constant hydraulic head (i.e. phreatic level) was assigned to the right nodes of the model, corresponding to a water table located at 0.8 m depth from the ground level. An impermeable boundary condition was applied to the base of the model. It is worth noticing that, on the river side, both hydraulic and climatic boundary conditions have been imposed to the calculation mesh, enabling to switch from time-variable pressure head to atmospheric coupling when the specified nodal pressure head is negative (i.e. when the hydrometric level is lower than the elevation of relevant nodes). Additional details on main impacting boundary conditions (e.g. rainfall and river water level) are also plotted in Figure 8(c).

5.2 Initial conditions

A suitable description of the initial conditions, here defined in terms of pressure head distribution, represents another crucial step for water flow modelling. For transient seepage analyses, any initial assumption required, which may be quite arbitrary, will in many cases strongly affect the final outcome (Sleep and Duncan, 2013). For the present study, two different scenarios were investigated: case (a) a non-linear soil suction distribution based on a spatial extrapolation of the observed pore-water pressure data (including suction) and case (b) a hydrostatic profile of soil suction above the phreatic level.

Although a hydrostatic profile above the water table is typically the assumption adopted in common practice, the measured distribution does not follow this trend. Jafari et al. (2019) showed by means of numerical simulations that coupling soil-atmosphere boundary conditions with precipitations events, a rather uniform suction distribution within the embankment is obtained. However, the pore-water pressure/suction profile with depth measured within the studied river embankment is rather different, as seen in Figure 10. In order to obtain a representative initial spatial distribution of suctions, a number of field data collected on December 1st 2017 was therefore used to extrapolate the values throughout the domain of analysis using the well-established Kriging method (Krige, 1951). Namely five dielectric sensors (MPC1, MPC3, SPC1 and MPB2), two tensiometers (TB1 and TC1) and two piezometers (from a pre-existing monitoring system) were considered. This geostatistical algorithm was formalised by Matheron (1962), based on Krige's empirical work for evaluating mineral resources. The approach is able to extend spatially distributed data to a whole region of interest, thus providing the initial conditions all over the model domain. As a general rule, the values of suction integrated in the model were considered only if their value was less than the hydrostatic distribution as defined by the deeper suction measurement. This criterion was relevant only for shallow measurements (MPC2, SPB1 and MPB2), where suction values raise up to thousands kPa, while all the other monitoring suction data are always lower than this cut-off. This procedure was necessary to avoid that extremely high suction values skewed the interpolation results.

For the Kriging interpolation to define the initial conditions, seven additional points were considered besides the nine directly measured. These are in agreement with the boundary conditions used in the transient seepage analysis model. In particular, the hydrometric level on the river side of the model and the groundwater table depth as measured by piezometers on the landward area. Finally, the top ground boundary conditions in Figure 10, on the embankment crest and on two points along the levee slopes, were used to perform the Kriging interpolation, where the suction values were extrapolated assuming a hydrostatic distribution starting from the closest suction measurement point.

In particular, in Figure 10 the pore-water pressure distribution obtained by the Kriging and used as initial conditions for transient seepage analyses is showed through isolines every 10 kPa, highlighting the $u=u_a-u_w$ = 0 kPa with a bold dotted line, where monitoring data used as input both from the berm and from the crest are also shown. In order for the appropriate suction distribution to develop, especially near the ground surface because of soil-atmosphere interaction, the starting point was selected to allow for a spin-up period of two weeks, before the first significant hydrometric peak impacts the levee.

5.3 Comparison of experimental data and water flow numerical results

Figure 11 presents the results of numerical seepage analyses in terms of pore-water pressure/suction values together with data collected in situ for the same period and hydrometric level fluctuations. Comparison is made at a selection of points where sensors are installed, i.e. at depths ranging from 4.6 to 17 m from the embankment crest and 4.8 m from the berm surface level. Substantial agreement between the monitored (symbols) and numerical (lines) results is observed for the whole time period, which validates the transient flow model developed. Sensitivity studies performed on the saturated permeability of the levee allowed to improve the accuracy of the numerical model by using the monitoring data as observation points for an objective function to be minimized.

At peak river water level (December 13th 2017), the transient seepage analysis provides a good fitting of the hydraulic and retention response of the levee to hydrometric fluctuations and climatic conditions. There are some differences among numerical and monitoring data for TB1: a possible explanation is that the sensor installed in the berm becomes submerged during high water events and it is plausible that water filled the protection tubes where the tensiometer is placed. Therefore, during high water events it would be better to refer directly to the river water levels for this point. However, such discrepancy appeared only for this specific event.

Differences in suction values appear in the period March 14th 2018 – April 30th 2018, which is characterised by a considerable persistence of hydrometric peaks. In this period, the model tends to provide higher water retention, even though the magnitude and trend of suction variations are generally still comparable. Such partial discrepancy could be partly ascribed to the hysteresis effect that was observed under cyclic loading conditions, but was not implemented in the hydraulic soil model. In fact, hysteresis of the soil water retention curve can induce greater changes in suction values, as variations can occur in the area enclosed by the main drying and wetting curves (Liu et al. 2017). With regards to the core of the river embankment (e.g. MPC1 at 4.6 m depth), the modelled suction shows limited variations for the whole observation period, in agreement with the observed data. This can be noticed also from Figure 12, where pore-water pressure/suction monitored values are plotted together with the numerical output for a specific time of analysis (March 14th 2018) in terms of a isoline map. Compared to the number of monitored data used to define the initial conditions in the Kriging, here an additional sensor TC2 had been installed and furthermore the piezometric readings from previously installed sensors are also presented. All these measurements confirm the transient seepage analysis results and together with the considerable agreement discussed in Figure 11 validate the transient flow model, thus allowing the implementation of related numerical analyses for the stability assessment.

6. Stability analysis of the river embankment under transient seepage conditions

Limit Equilibrium Analysis were performed using the numerical code SLOPE/W (Geo-Slope International Ltd, 2012b) to assess the stability of the river embankment during the period December 1st 2017 – April 30th 2018. In particular, only collapse mechanisms involving landward side instability have been investigated, being considerably critical for the specific water retaining infrastructure system and strongly dependent on pore-water pressure/suction values at depth. The adopted Morgenstern and Price Method (Morgenstern & Price 1965) makes use of the Newton-Raphson numerical technique to solve the moment and force equilibrium equations in order to obtain relevant Safety Factors (SF). The solution is based on the composition of tangential and normal forces to each slice, assuming a user defined mathematical function to describe the direction of interslice forces both for circular and composite-shape slip surfaces. In order to identify the slip surfaces that best represent a possible collapse mechanism with respect to overall stability, the following geometrical constraints were defined for slip surface generation: a minimum depth condition of 2 m, and within a 4 and 7 m range for the entry and exit points of trial slip surfaces at the top and at the toe of the slope, respectively. Pore-water pressure/suction distributions determined from the seepage analysis at each time-step provided the key input to perform limit equilibrium analyses. Shear strength was defined according to the Vanapalli failure criterion (Vanapalli et al. 1996), extending the classic Mohr-Coulomb criterion as:

7. $\tau = c' + (\sigma_n - u_a)\tan\varphi' + (u_a - u_w)S_e\tan\varphi'$

where c' = effective cohesion, σ_n = total normal stress, φ' = effective angle of shear resistance and all other parameters as previously defined. Unsaturated soil unit weights were calculated on the basis of the SWRCs for each Unit, based on the soil suction obtained from the numerical simulations and the saturated unit weight listed in Table 1, while soil strength parameters are as listed in Table 2.

Figure 13 shows the safety factors spatial distribution (Baker & Leshchinsky 2001) by means of Safety Maps for the time-steps identified in Figure 11 (circles), which represent potentially critical conditions for the considered period of study. Furthermore, it presents the pore-water pressure/suction distributions obtained by solving the transient seepage analyses. The model clearly shows both the location of the slip surface and the magnitude of critical SF values for each time-step selected. The subdivision of SF values by coloured zones has been defined considering (1) the most critical slip surface contour determined for the lowest SF at the last time-step of analysis, i.e. 1.425, and (2) three zones (differently grey-shaded) characterised by SF increments of 0.075. The most important observation is that lower safety margins do not correspond to maximum hydrometric peaks (a – 13/12/2017) or soon after their occurrence (b – 13/02/2018), but rather at the end of the wet season, as a consequence of persistent high-water levels (c – 14/03/2018 and d – 14/04/2018). Therefore, the stability conditions under transient seepage of these linear infrastructures not only depend on the current external water level, but also on the recent hydrometric time history. Note that due to the significant margin of safety available at the beginning of the analysis, the reduction in the SF value is not dramatic with respect to possible failure mechanisms in the levee. This is because typical conditions have been analysed, without being the most critical ever expected.

The behaviour observed is caused by the succession of high-water events that can give rise to a progressive reduction of suction values and therefore to both more limited contribution of partially saturated soil strength and an increase in permeability throughout the river embankment. The difference in SFs between the first and the last time-step considered is around 10%, highlighting the importance of considering the transient seepage processes for a reliable safety assessment in these linear infrastructures. Furthermore, it shows the importance of integrated monitoring for the validation of stability analyses, even though in this specific case the probability of failure is close to zero. For example, a 100,000 trials Monte Carlo simulation, which considers φ' as a probabilistic parameter based on the distributions in Figure 5 for Unit A and Unit B, provides a reliability index (Baecher & Christian 2003) β_d = 11.8, which corresponds to a very low probability of global failure, in correspondence of the lowest values of SFs computed (14/04/2018). Naturally, different sources of uncertainties should be taken into account (e.g. variability of soil retention and hydraulic properties), which may significantly affect the reliability index and the probability of failure. However, values of β_d lower than zero (i.e. average value of the safety factors distribution lower than one) have been obtained for river water-levels on 13/12/2017 and 13/03/2018, when using the simplistic assumption of steady-state assumption to quantify the stability conditions toward global collapse for the elapsed period of time. Thus demonstrating the excessively prudential estimation of safety margins.

With regards to the two different scenarios used as initial conditions, results in terms of critical safety factors are plotted in Figure 14, together with hydrometric levels. Case (a) is based on spatial interpolation of field monitoring data, while case (b) on a hydrostatic profile above the phreatic level, as previously described. Differences in SF values for cases (a) and (b) vary from 0.015 to 0.10, from the initial to the final time-step, which shows the importance of initial conditions – typically unknown – on the overall stability assessment.

A further comparison of SF values, based on the same initial conditions (hydrostatic profile of soil suction) but different values of the saturated permeability for Unit A is also presented in Figure 14. For cases (a) and (b), k_{sat} was calibrated to match the monitoring data – as previously explained. In case (c), k_{sat} was based only on laboratory and field testing information. It can be seen how even relatively small differences of k_{sat} can possibly affect SF values and their variability with time. Due to the unavoidable uncertainty in the determination of such a crucial parameter, its calibration performed on a consistent set of reliable monitoring data can thus enhance the reliability of stability analyses.

Conclusions

Reliable estimates of actual failure probabilities for existing river embankments under continuously changing boundary conditions represent an ever-demanding task for researchers and designers alike, as well as for those involved in their maintenance and management. Standard methods of analysis are still based on the supposedly conservative assumption of steady-state conditions within the embankment. However, this design criterion begins to be questioned as changes in climate modify the loads imposed on earthen water retaining infrastructures. Possible increases in soil shear strength due to suction are typically taken into account by introducing apparent cohesion above the phreatic level. Indeed, this can lead to unrealistic results and does not contribute towards calculating the actual margins of safety toward global collapse. Because water flow is in fact in transient conditions at all times, knowledge of soil suction and water content distributions is key to a realistic assessment of the existing safety conditions and it is crucial to tackle any uncertainty with regards to spatial and temporal variability. For the advanced analysis and design of linear earthen infrastructures, the partially saturated state of the embankment materials must be taken into account and the related soil state parameters must be suitably defined. In this respect, specialist integrated monitoring is functional to calibrate predictive analyses and enhance their reliability and coherency.

In the present study, extensive site investigation and thorough geotechnical characterization guided the installation of various probes for the direct and indirect measurement of soil water content and suction at different meaningful depths within the earthen structure, both in the core and in the shoulder of an existing embankment section of the river Secchia (Northern Italy). Data collected and relevant research activities, still ongoing, mainly aim at estimating the soil hydraulic and retention response for the instrumented river embankment. These provided an important source of knowledge to realistically assess transient seepage and stability conditions for the specific infrastructure, requiring only one variable to be calibrated (k_{sat}). Considerable agreement was obtained between numerical and monitored pore-water pressure/suction distributions when using site-representative initial conditions, here implemented through a rather novel procedure, validating the methodology developed.

The most important finding is that the stability conditions under transient seepage are significantly influenced by the recent hydrometric time history. In particular, the lowest SF values are not necessarily in correspondence of the peak water level and high-water persistence is equally if not more important. Basing risk assessments on the current external water level only, as traditionally done, can therefore lead to overestimation of the SF. In the present case, neglecting recent hydrometric time history would lead to about 0.15 higher values in SF between 16/03/2018 and 01/05/2018. Furthermore, site measurements showed that the traditionally assumed hydrostatic suction distribution above the phreatic level is not realistic and can be unconservative.

The monitoring system configuration proposed herein could be replicated, with small adaptations, to any section of similar flood embankments. However, it is self-evident that such experimental set-up cannot be implemented in each critical section over long linear stretches of river embankments and therefore a suitable way of extending the experimental findings is required. In principle, established technologies already typically used for river embankment monitoring - like optic fibers or integrated geophysical methods – could be calibrated and guide interpretation based on reliable local data. Further efforts should be then devoted to the extension of such methodology to long stretches of river embankments and, eventually, to the implementation of an early-warning system against flooding risk in relation to possible river embankment failures.

Data Availability Statement

Monitoring and laboratory data, as well as the results obtained from seepage and stability numerical analyses, all supporting the findings of the present study, are owned by the Authors and can be made available from the corresponding author upon reasonable request.

Acknowledgements

This work is part of the INFRASAFE project activities, funded under the POR FESR 2014-2020 scheme, whose grant is gratefully acknowledged.

References

Baecher GB and Christian JT (2003). Reliability and statistics in geotechnical engineering. John Wiley & Sons, Ltd, Chichester, England.

Baker R and Leshchinsky D (2001). Spatial Distribution of Safety Factors. Journal of Geotechnical and Geoenvironmental Engineering **127**: 135–45.

Bittelli, M (2011). Measuring Soil Water Content: A Review. Hortechnology **21(3)**: 293–300.

Calabresi G, Colleselli F, Danese D, Giani G, Mancuso C, Montrasio L, Nocilla A, Pagano L, Reali E, Sciotti A (2013). Research study of the hydraulic behaviour of the Po River embankments. Canadian Geotechnical Journal **50(9)**: 947–960.

Casagli N, Rinaldi M, Gargini A and Curini A (1999). Pore Water Pressure and Streambank Stability:

Results from a Monitoring Site on the Sieve River, Italy. Earth Surface Processes and Landforms **24(12)**: 1095–1114.

Cascini L, Sorbino G, Cuomo S and Ferlisi S (2014). Seasonal effects of rainfall on the shallow pyroclastic deposits of the Campania region (southern Italy), Landslides **11**, 779-92.

D’Alpaos L, Brath A, Fioravante V, Gottardi G, Mignosa P and Orlandini S (2014). Relazione Tecnico-Scientifica Sulle Cause Del Collasso Dell ’ Argine Del Fiume Secchia Avvenuto Il Giorno 19 Gennaio 2014 Presso La Frazione San Matteo. See http://Ambiente.Regione.Emilia-Romagna.it/geologia/notizie/notizie-2014/fiume-Secchia (accessed 01/12/2018).

Decagon Devices (2016a). GS3. Water Content, EC and Temperature Sensors. Decagon Devices, Inc. Pullman, WA, United States.

Decagon Devices (2016b). MPS-2 & MPS-6. Dielectric Water Potential Sensors. Decagon Devices, Inc. Pullman, WA, United States.

Delta-T Devices (2016). SM150T. Soil Moisture Sensor. Delta-T Devices, Cambridge, UK.

Duncan JM (2000). Factors of Safety and Reliability in Geotechnical Engineering. Journal of Geotechnical and Geoenvironmental Engineering 1**26(4)**: 307–16. doi/10.1061/%28ASCE%291090-241%282000%29126%3A4%28307%29.

Fredlund DG, Morgenstern NR and Widger RA (1978). Shear strength of unsaturated soils. Canadian Geotechnical Journal **15(3)**: 313-321.

Geo-Slope International Ltd (2012a). Stability Modelling with SLOPE/W 2012. Geo-Slope International Ltd., Calgary, Canada.

Geo-Slope International Ltd (2012b). Vadose Zone Modelling with VADOSE/W 2012. Geo-Slope International Ltd., Calgary, Canada.

Gottardi G, Gragnano CG, Rocchi I and Bittelli M (2016). Assessing River Embankment Stability Under Transient Seepage Conditions. Procedia Engineering **158**: 350-55. doi/10.1016/j.proeng.2016.08.454

Gottardi G and Gragnano CG (2016). On the role of partially saturated soil strength in the stability analysis of a river em-bankment under steady-state and transient seepage conditions. In *Proceedings of 3rd European Conference on Unsaturat-ed Soils – E-UNSAT 2016*, Paris, France.

Gottardi G, Gragnano CG, Ranalli M, Tonni L (2020). Reliability analysis of riverbank stability accounting for the intrinsic variability of unsaturated soil parameters. Natural Hazard, **86(2020)**: 101973.

Gragnano CG (2017). Numerical and Experimental Investigation into the Effect of Retention Properties of Partially Saturated Soils for the Stability Analysis of River Embankments. PhD dissertation, University of Bologna, Italy. doi:10.6092/unibo/amsdottorato/8193.

Gragnano CG, Rocchi I, Moscariello M, Cuomo S and Gottardi G (2018). Laboratory measurement of the mechanical and retention properties of a river embankment silty soil in partially saturated condition. In *Proceedings 7th International Conference on Unsaturated Soils – UNSAT 2018*, Hong Kong.

Gragnano CG, Moscariello M, Cuomo S, Rocchi I and Gottardi G (2019). Experimental study on a partially saturated soil of a river embankment. In *Proceedings 17th European Conference on Soil Mechanics and Geotechnical Engineering – XVII ECSMGE-2019*, Reykjavik, Iceland.

Griffiths DV and Lane PA (1999). Slope stability analysis by finite elements, Géotechnique **49(3)**: 387-403.

Harris J, Davenport F and Lehane B (2013). Seasonal variations of soil suction profiles in the Perth metropolitan area, Australian Geomechanics Journal **48(2)**: 65-73.

Jafari NH, Cadigan JA, Stark TD and Woodward PE (2019). Phreatic surface migration through an unsaturated levee embankment. Journal of Geotechnical and Geoenvironmental Engineering **145(11)**: 05019010.

Jasim FH, Vahedifard F, Ragno E, AghaKouchak A and Ellithy G (2017). Effects of climate change on fragility curves of earthen levees subjected to extreme precipitations. In *Proceeding, Geo-risk 2017: Geotechnical Risk from Theory to Practice*, Reston, VA: ASCE.

Johansen o (1975). Thermal conductivity of soils. PhD dissertation, Trondheim, Norway (CRREL Draft

Translation 637, 1977), ADA 044002.

Johnston GH, Ladanyi B, Morgenstern NR and Penner E (1981). Engineering characteristics of frozen and thawing soils. In: Permafrost: Engineering design and construction. Wiley, New York: 73-147

Krige DG (1951). A statistical approach to some basic mine valuation problems on the Witwatersrand. Journal of the Southern African Institute of Mining and Metallurgy **52(6)**: 119-39.

Kriste B, Iden SC and Durned W (2019). Determination of the Soil Water Retention Curve around the Wilting Point: Optimized Protocol for the Dewpoint Method. Soil Science Society of America Journal. doi:10.2136/sssaj2018.08.0286.

Kulhawy FH and Mayne PW (1990). Manual on Estimating Soil Properties for Foundation Design. Electric Power Research Institute EL-6800, Project 1493-6, Electric Power Research Institute, Palo Alto, California

Liu SY, Shao LT and Li HJ (2015). Slope stability analysis using the limit equilibrium method and two finite element methods. Computers and Geotechnics **63**: 291-98

Liu K, Vardon PJ, Hicks MA and Arnold P (2017). Combined Effect of Hysteresis and Heterogeneity on the Stability of an Embankment under Transient Seepage. Engineering Geology **219**: 140–50.

Mayne PW and Campanella RG (2005). Versatile Site Characterization by Seismic Piezocone. In *Proceedings of the 16th International Conference on Soil Mechanics and Geotechnical Engineering* – ICSMGE, Osaka. **2**: 721-724.

Matheron G (1962). Traité de geostatisque appliquée, vol. I: Memoires du Bureau de Recherches Géologiques et Miniéres, no. 14, Editions Technip, Paris, France.

Morgenstern NR and Price VE (1965). The Analysis of the Stability of General Slip Surfaces. Géotechnique **15(1)**: 79–93.

Mouyeaux A, Carvajala C, Bressolette P, Peyrasa L, Breul P and Bacconnet C (2018). Computers and Geotechnics Probabilistic Stability Analysis of an Earth Dam by Stochastic Finite Element Method Based on Field Data. Computers and Geotechnics **101**: 34–47, doi.org/10.1016/j.compgeo.2018.04.017.

Mualem Y (1976). A New Model for Predicting the Hydraulic Conductivity of Unsaturated Porous Media. Water Resources Research **12(3)**: 513–22.

Nguyen Q, Fredlund DG, Samarasekera L and Marjerison BL (2010). Seasonal pattern of matric suctions in highway subgrades, Canadian Geotechnical Journal **47(3)**: 267-80.

Orlandini S., Moretti G and Albertson JD (2015). Evidence of an Emerging Levee Failure Mechanism Causing Disastrous Floods in Italy. Water Resources Research **51(10)**: 7995–8011.

Penman HL (1948). Natural evaporation from water, bare soil and grass. In *Proceedings of the Royal Society of London. Series A*. **193**: 120-45.

Peters, A. and W. Durner (2008): Simplified Evaporation Method for Determining Soil Hydraulic Properties, Journal of Hydrology **356**: 147–162, doi:10.1016/j.jhydrol.2008.04.01668.

Pozzato A, Tarantino A, De Polo F (2014). Analysis of the effects of the partial saturation on the Adige river embankment stability. *Proceedings of the 6th International Conference on Unsaturated Soils, UNSAT 2014*. **2**: 1367-1372.

Ridley A, McGinnity B and Vaughan P (2004). Role of Pore Water Pressures in Embankment Stability. Geotechnical Engineering **157(4)**: 193–98, doi/10.1680/geng.2004.157.4.193.

Rinaldi M, Casagli N, Dapporto S and Gargini A (2004). Monitoring and Modelling of Pore Water Pressure Changes and Riverbank Stability during Flow Events. Earth Surface Processes and Landforms **29(2)**: 237–54.

Rivera-Hernandez XA, Ellithy GS and Vahedifard F (2019). Integrating Field Monitoring and Numerical Modeling to Evaluate Performance of a Levee under Climatic and Tidal Variations. Journal of Geotechnical and Geoenvironmental Engineering **145(10)**: 05019009

Robertson PK and Cabal (Robertson) KL (2012). Guide to Cone Penetration Testing for Geotechnical Engineering. Gregg Drilling & Testing.

Robertson PK (2009). Interpretation of cone penetration tests - a unified approach. Canadian Geotechnical Journal **46(11)**: 1337-1355.

Rocchi I, Gragnano CG, Govoni L, Mentani A, Bittelli M, Castiglione P, Buzzi O and Gottardi G (2018a).

A new technique for deep in situ measurements of soil water retention properties. Geotechnical Research **5(1)**: 1-10.

Rocchi I, Gragnano CG, Govoni G, Gottardi G and Bittelli M (2018b). In-situ measurements of soil water content and suction to assess river embankments stability under transient flow conditions. In *Proceedings 7th International Conference on Unsaturated Soils – UNSAT 2018*, Hong Kong.

Rocchi I, Gragnano CG, Govoni L, Bittelli M, Gottardi G (2020). Assessing the performance of a versatile and affordable geotechnical monitoring system for river embankments. Physics and Chemistry of the Earth, Parts A/B/C, doi/10.1016/j.pce.2020.102872.

Schelle H, Heise L, Janicke K and Durner W (2013). Water Retention Characteristics of Soils over the Whole Moisture Range: A Comparison of Laboratory Methods. European Journal of Soil Science **64**: 814–21.

Schindler U, Durner W, Von Unold G and Mueller L (2010). Evaporation Method for Measuring Unsaturated Hydraulic Properties of Soils : Extending the Measurement Range. Soil Physics **74(4)**: 1071–83.

Schindler U, Mueller L, da Veiga M, Zhang Y, Schlindwein S and Hu C (2012). Comparison of Water-Retention Functions Obtained from the Extended Evaporation Method and the Standard Methods Sand / Kaolin Boxes and Pressure Plate Extractor. Journal of Plant Nutrition and Soil Science **175(4)**: 527–34.

Sleep MD and Duncan JM (2013). Effects of initial conditions on the results of transient seepage analyses. In: ASCE, editor. *Proceedings Geo-Congress 2013: Stability and Performance of Slopes and Embankments III*, San Diego, California, US. 1081–91.

Smethurst JA, Clarke D and Powrie W (2006). Seasonal changes in pore water pressure in a grass-covered cut slope in London Clay. Géotechnique **56(8)**: 523–37.

Stark TD, Jafari NH, Lopez-Zhindon S and Baghdady A (2017). Unsaturated and transient seepage analysis of San Luis Dam. Journal of Geotechnical and Geoenvironmental Engineering **143(2)**: 04016093.

Tanoue M, Hirabayashi Y and Ikeuchi H (2016). Global-scale river flood vulnerability in the last 50 years. Scientific Reports 6: 3-9. https://doi.org/10.1038/srep36021.

Tarantino A and Pozzato A (2008). Instruments for monitoring the unsaturated zone (in Italian). *Italian Geotechnical Journal*. **3**: 109-21.

Toll DG, Mendes J, Hughes PN, Glendinning S and Gallipoli D (2012). Climate Change and the Role of Unsaturated Soil Mechanics. Geotechnical Engineering Journal of the SEAGS & AGSSEA. **43(1)**: 76-82.

Toll DG, Lourenço SDN, Mendes J, Gallipoli D, Evans FD, Augarde CE, Cui YJ Tang AM, Rojas JC, Pagano L, Mancuso C, Zingariello C and Tarantino A (2016). Soil Suction Monitoring for Landslides and Slopes. Quarterly Journal of Engineering Geology and Hydrogeology **44(1)**: 23–33. doi/10.1144/1470-9236/09-010.

UMS (2011). T8. Long-term Monitoring Tensiometer. UMS GmbH, Münchenm Germany.

Vacondio R, Aureli F, Ferrari A, Mignosa P and Dal Palù A (2016). Simulation of the January 2014 Flood on the Secchia River Using a Fast and High-Resolution 2D Parallel Shallow-Water Numerical Scheme. Natural Hazard **80(1)**: 130–25.

van Genuchten MT (1980). A Closed-Form Equation for Prediccting Hydraulic Conductivity of Unsaturated Soils. Soil Science Society of America Journal **44(5)**: 892–98.

Vahedifard F, Williams JM and AghaKouchak A (2018). Geotechnical engineering in the face of climate change: Role of multi-physics processes in partially saturated soils. In *Proceedings IFCEE 2018 GSP No. 295*. Reston, VA: ASCE.

Vanapalli SK, Fredlund DG, Pufahl DE and Clifton AW (1996). Model for the Prediction of Shear Strength with Respect to Soil Suction. Canadian Geotechnical Journal **33(3)**: 379–92, doi/abs/10.1139/t96-060.

Yang H and Russell AR (2016). Cone penetration tests in unsaturated silty sands. Canadian Geotechnical Journal **53(3)**: 431-44.

Wilson GW (1990). Soil evaporative fluxes for geotechnical engineering problems. PhD dissertation,

University of Saskatchewan, Saskatoon, Canada.

List of figures

Figure 1. Pictures of the breach and flooded area during the river Secchia embankment collapse in January 2014.

Figure 2. Site location of the investigated river section and relevant CPTU performed.

Figure 3. (a) Stratigraphic model and (b) CPTU log profiles. NB. The hydrostatic pore pressure (u_0) presented in Fig. 3(b) are based on the piezometric water table measured at the time of testing (28-29 July 2016).

Figure 4. Soil water retention curves from reconstituted and undisturbed soil samples in the laboratory and from field installations: (a and c, same legend) from the crest of the embankment and (b and d, same legend) from the berm of the embankment, along drying (a and b) and wetting branches (c and d) for the field measurements only.

Figure 5. Unit A and B shear strength angles from CPTUs interpretation (solid lines) and relevant Gaussian probability density distribution (dashed lines).

Figure 6. Monitoring system installed in the river embankment section.

Figure 7. (a) Sketch and pictures (b and c) of the sensor installation techniques for coupled measurement of water content and hydraulic potential (suction).

Figure 8. Monitoring data in the period December 1^{st} 2017 – April 30^{th} 2018. (a) Pore-water pressure measured for deep sensors and hydraulic water level, (b) pore-water pressure measured for shallow sensors and (c) climatic data.

Figure 9. FE mesh, material distribution and boundary conditions.

Figure 10. Pore-water pressure/suction distribution on December 1^{st} 2017 (model initial conditions) considering spatial distribuion from field monitoring data.

Figure 11. Comparison of experimental field (symbols) and numerical (lines) data of the pore-water pressure/suction for the period December 1^{st} 2017 – April 30^{th} 2018.

Figure 12. Comparison of pore-water pressure/suction monitored values and results of transient seepage analysis on March 14^{th} 2018.

Figure 13. Safety map and pore-water pressure/suction distribution for selected critical time steps.

Figure 14. Variation with time of critical Safety Factors with different assumptions on initial conditions and k_{sat} for Unit A, i.e. spatial distribution from field monitoring data and k_{sat} calibrated from monitoring data (case (a)), hydrostatic distribution above the phreatic level and k_{sat} calibrated from monitoring data

(case (b)) and hydrostatic distribution above the phreatic level and k_{sat} estimated from experimental test (case (c)) for the period December 1st 2017 – April 30th 2018.

List of Tables

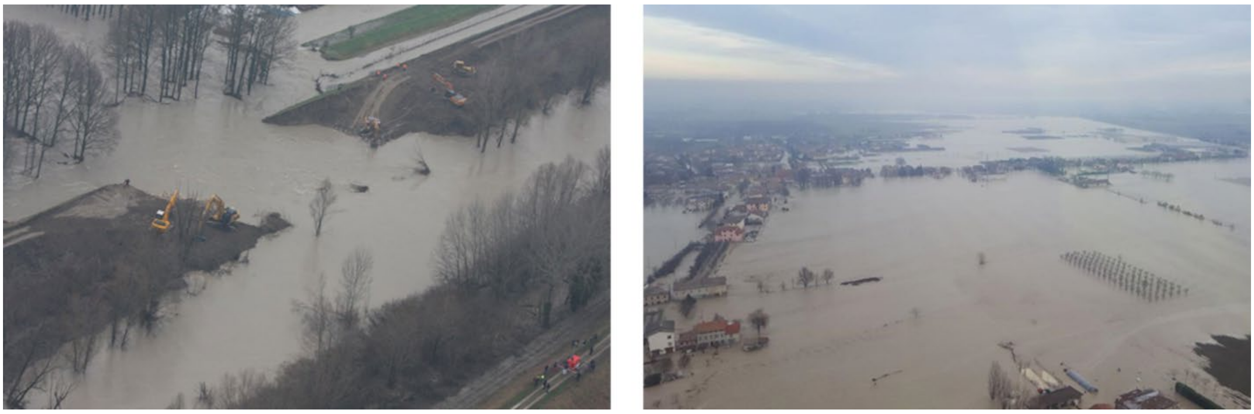

Figure 1

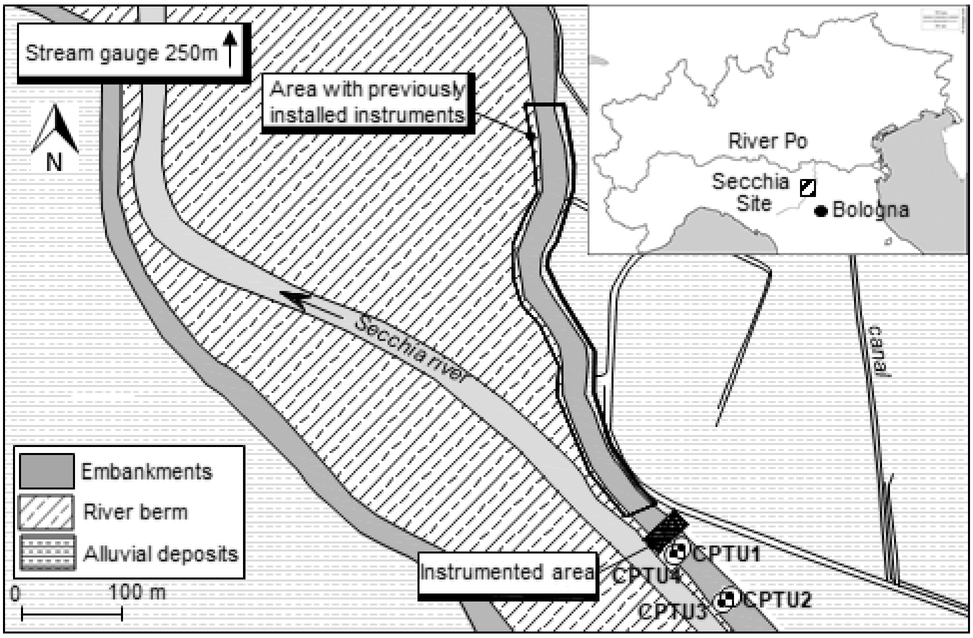

Figure 2.

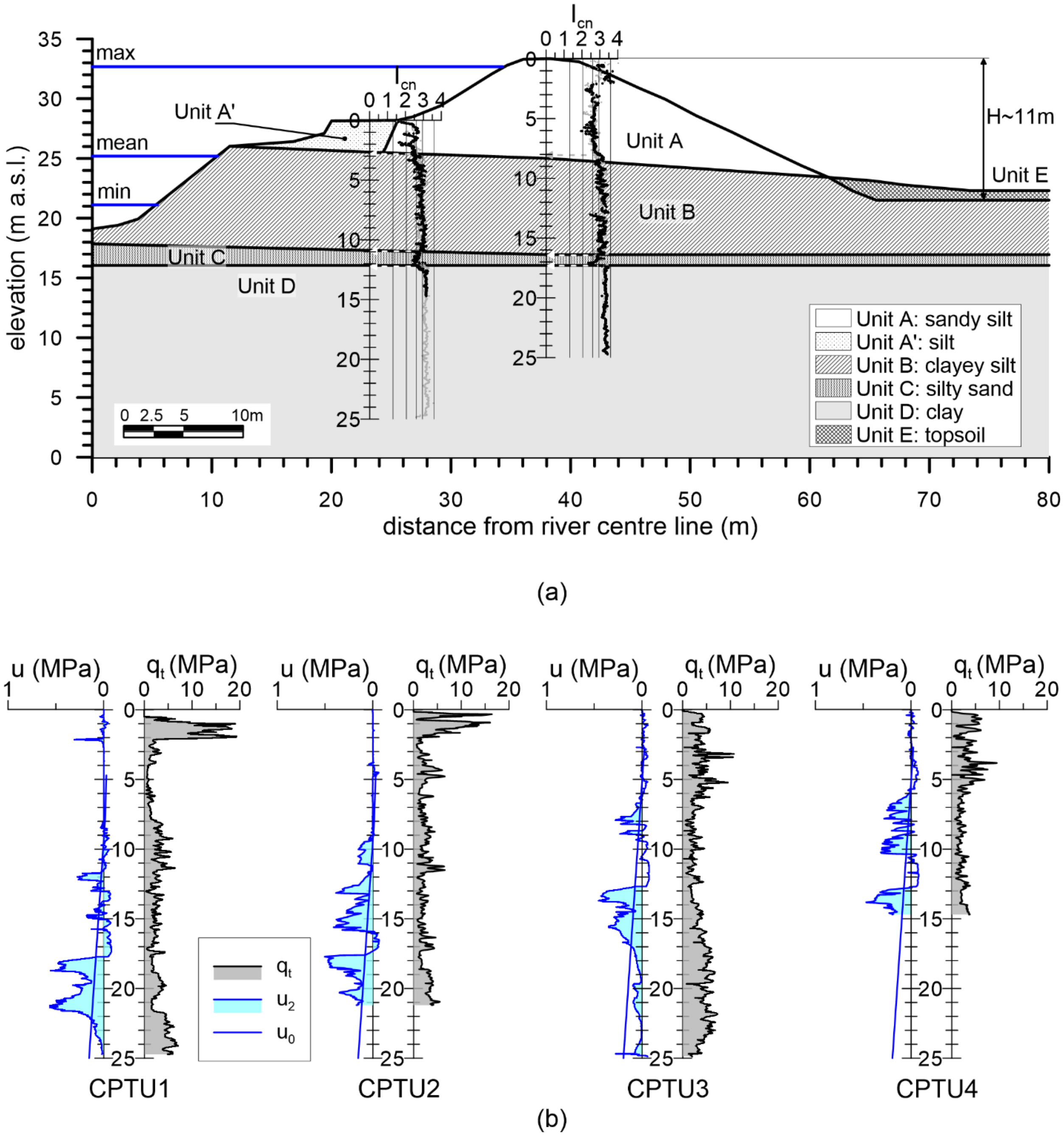

Icn
0 1 2 3 4
max
mean
min
Unit A'
Unit A
Unit B
Unit C
Unit D
Unit E
H~11m
elevation (m a.s.l.)
distance from river centre line (m)
0 2.5 5 10m
Unit A: sandy silt
Unit A': silt
Unit B: clayey silt
Unit C: silty sand
Unit D: clay
Unit E: topsoil
(a)
u (MPa)
qt (MPa)
qt
u2
u0
CPTU1
CPTU2
CPTU3
CPTU4
(b)

Figure 3.

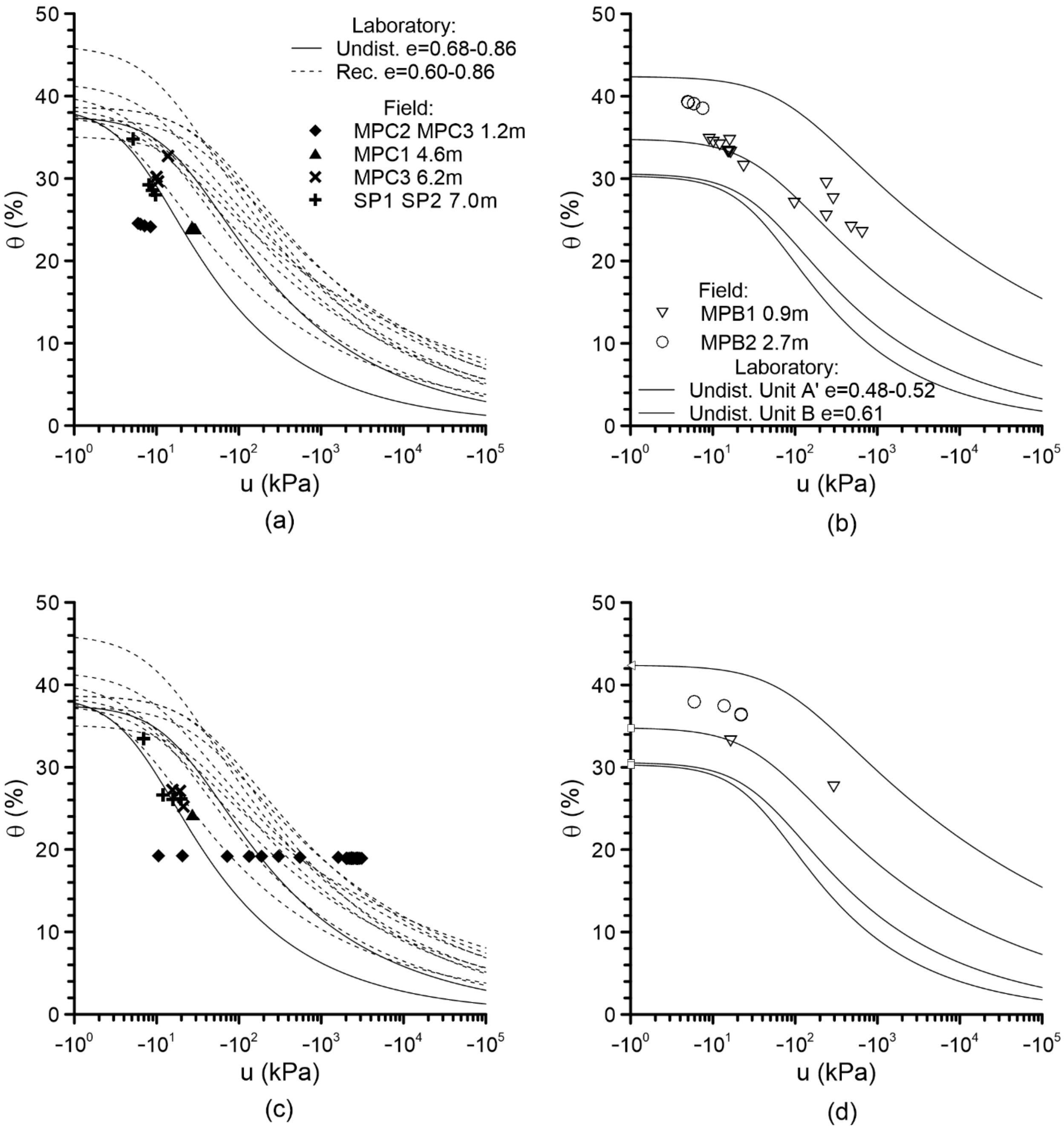

Figure 4.

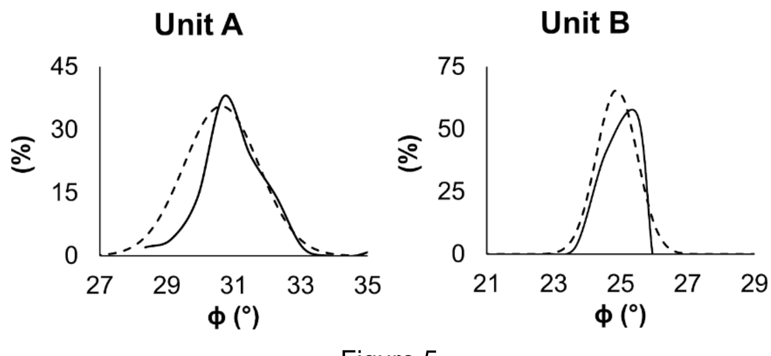

Figure 5

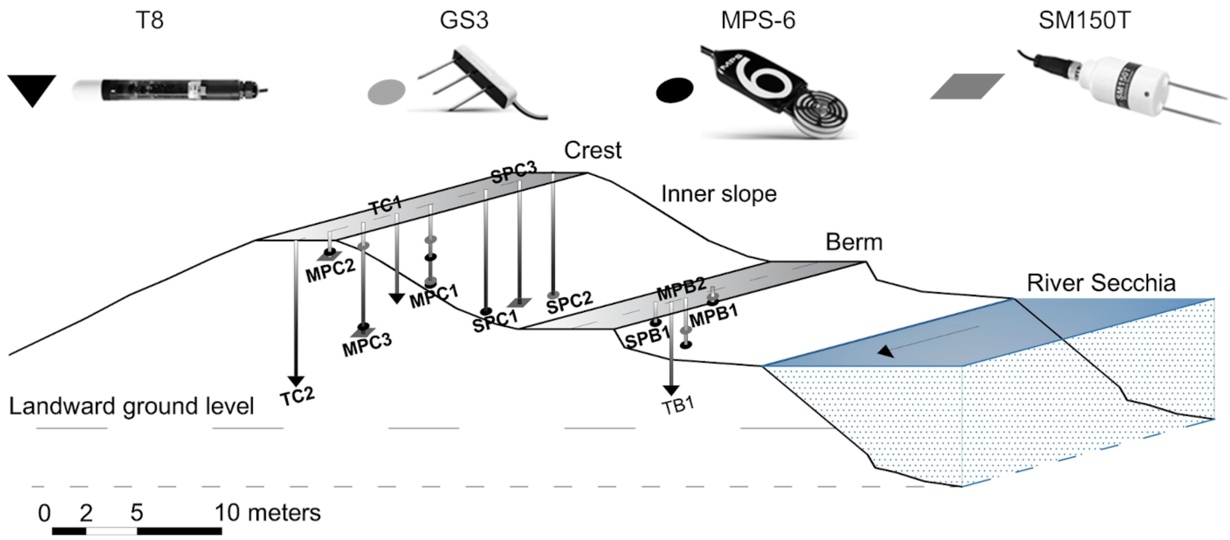

Figure 6.

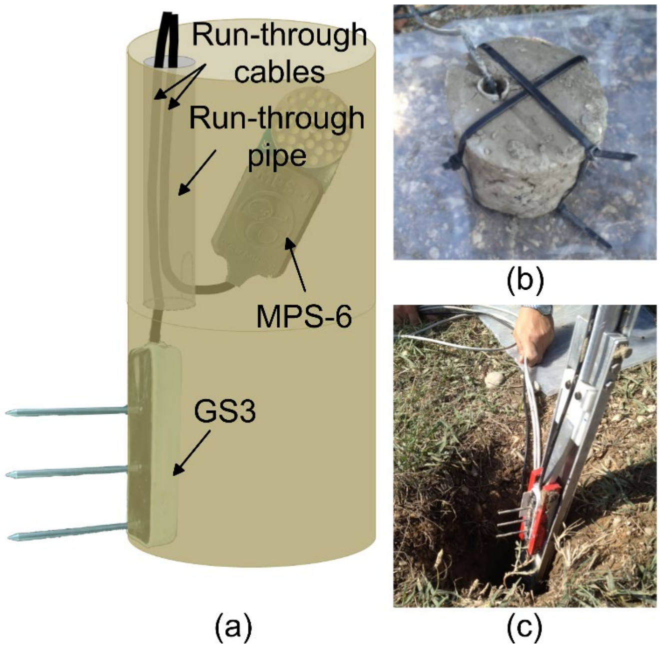

Figure 7.

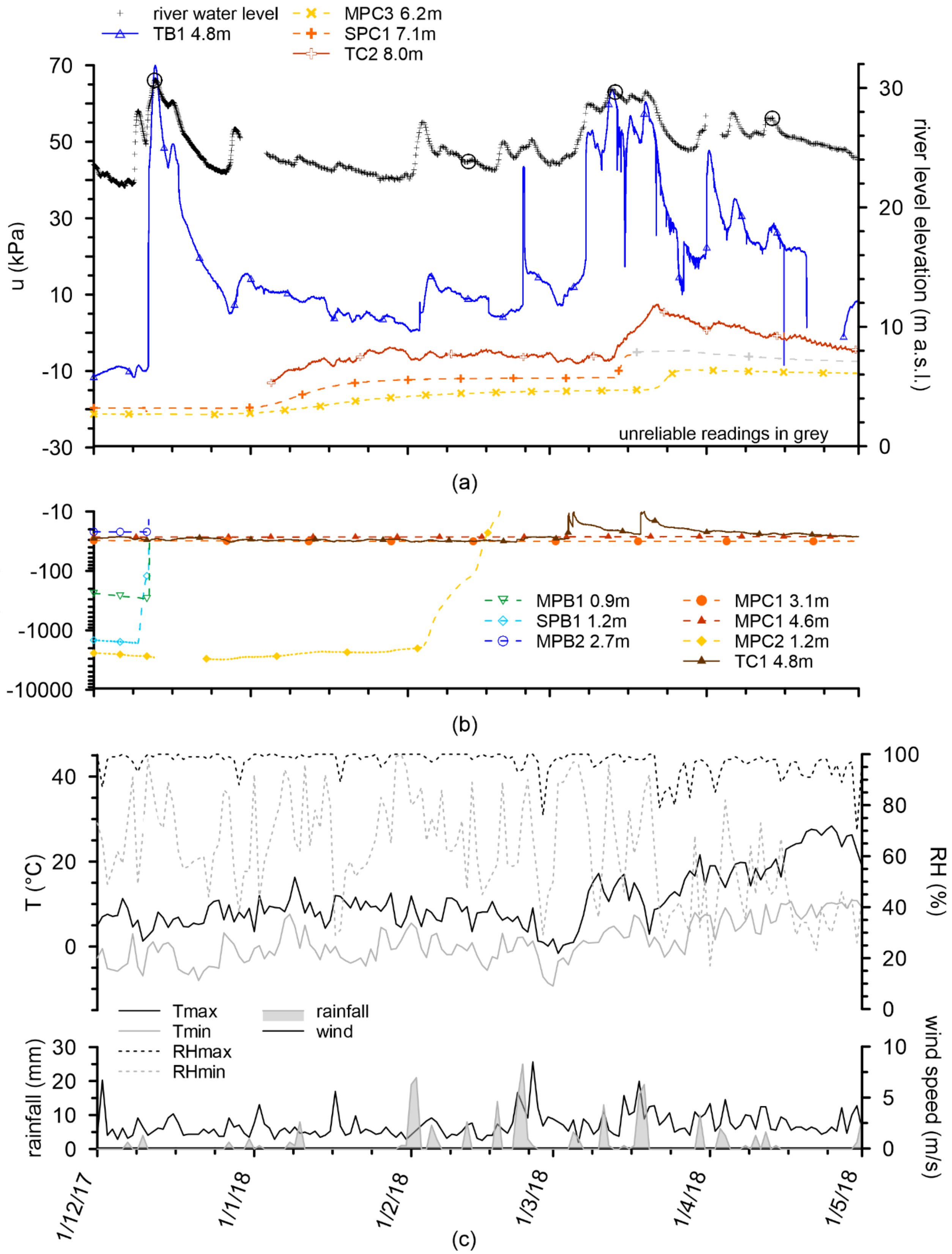
river water level
TB1 4.8m
MPC3 6.2m
SPC1 7.1m
TC2 8.0m
u (kPa)
river level elevation (m a.s.l.)
unreliable readings in grey
(a)
MPB1 0.9m
SPB1 1.2m
MPB2 2.7m
MPC1 3.1m
MPC1 4.6m
MPC2 1.2m
TC1 4.8m
u (kPa)
(b)
Tmax
Tmin
RHmax
RHmin
rainfall
wind
T (°C)
RH (%)
rainfall (mm)
wind speed (m/s)
1/12/17
1/1/18
1/2/18
1/3/18
1/4/18
1/5/18
(c)

Figure 8.

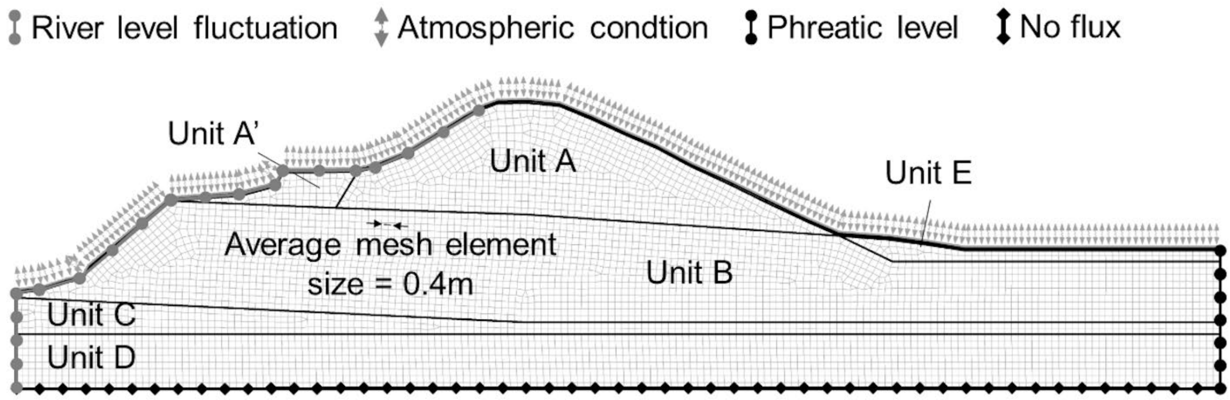

Figure 9

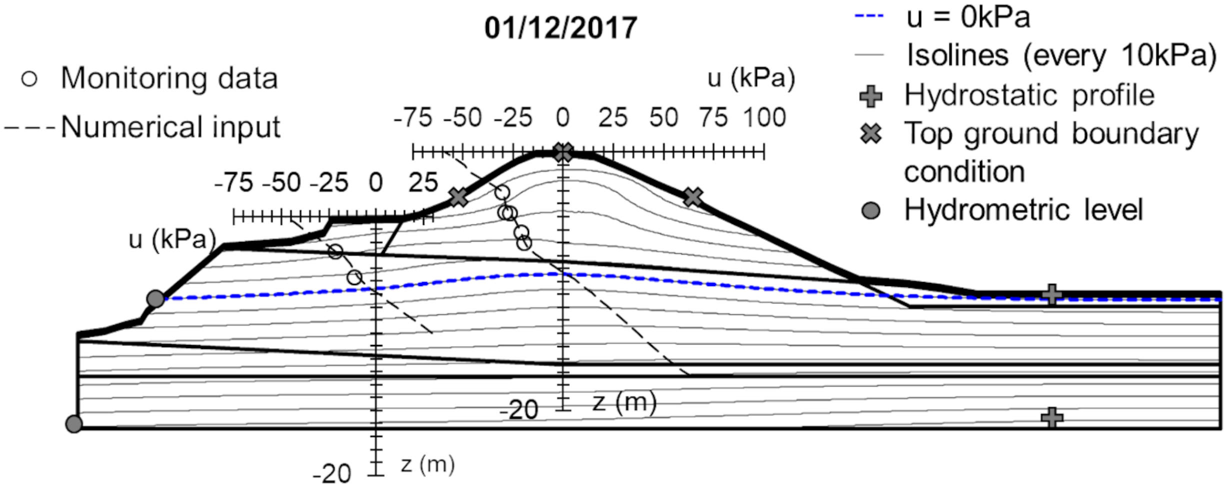

Figure 10.

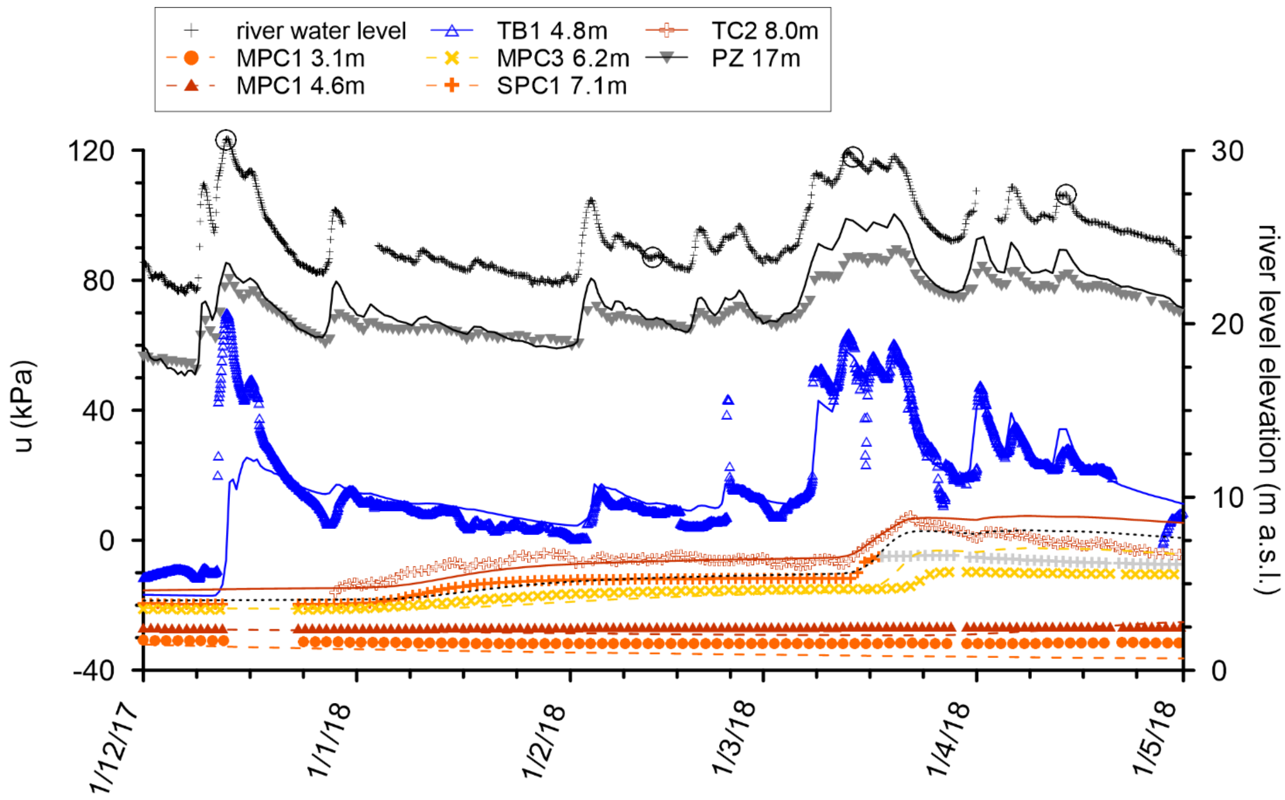

Figure 11.

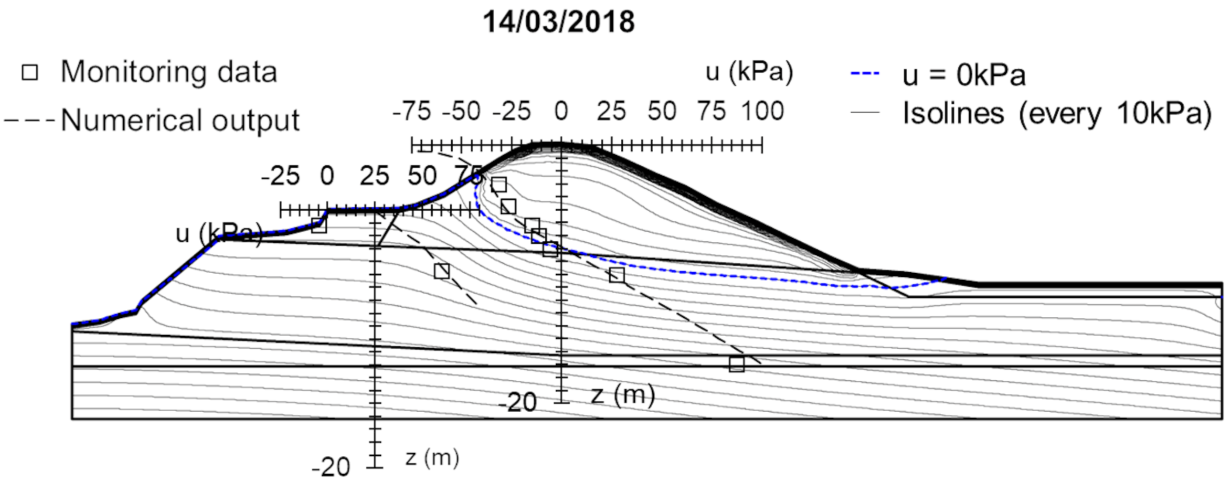

Figure 12

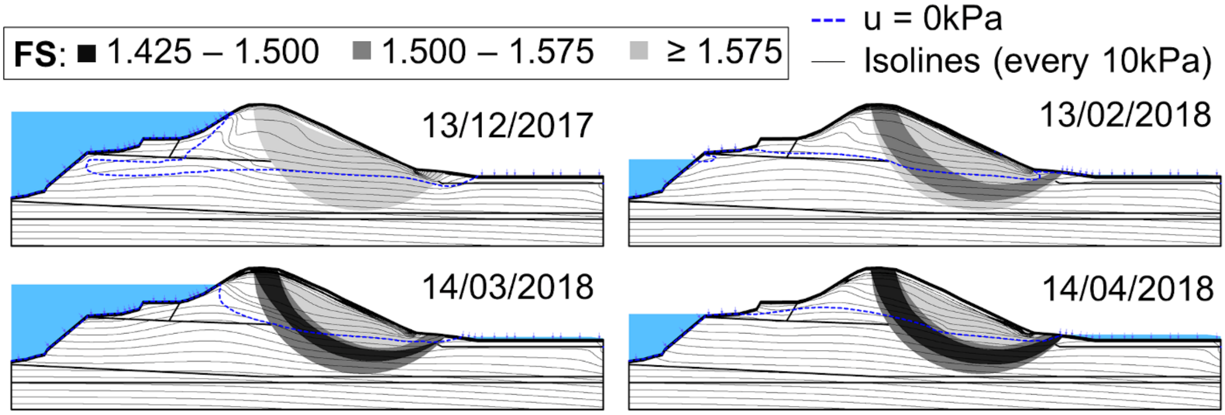

Figure 13.

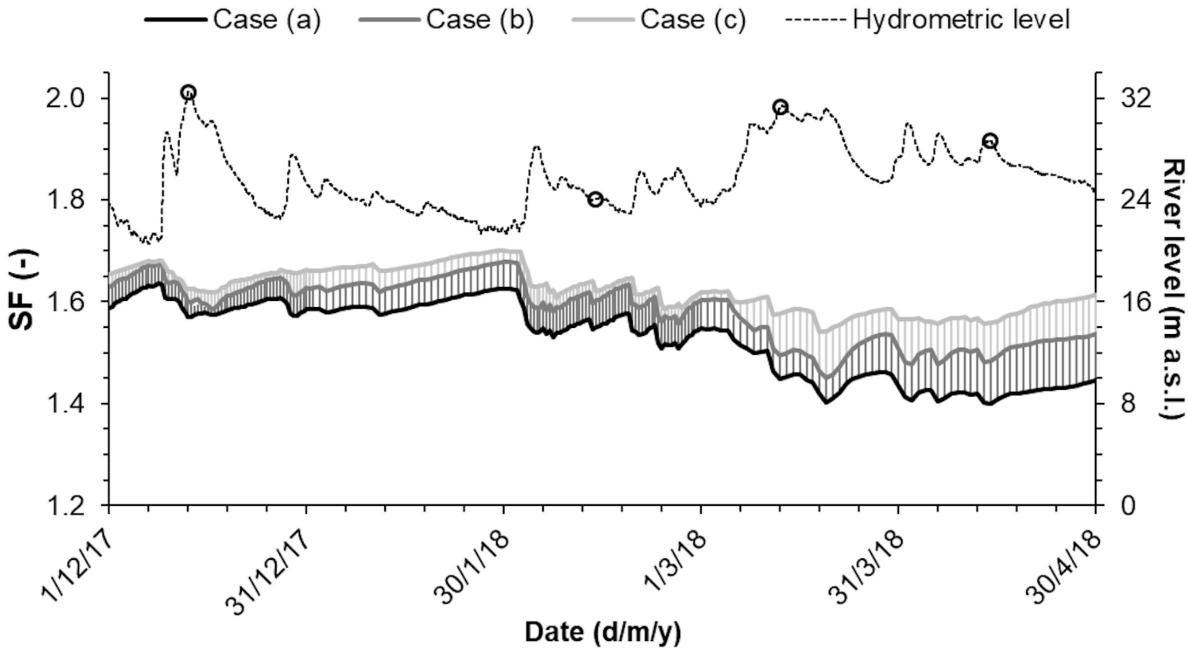

Figure 14.

Soil unit	D_{50}	D_{10}	c_u	c_c	FF	I_P	w_{LL}	G_s	γ_{sat}
-	mm	mm	-	-	%	%	%	-	kN/m³
Unit A	0.097	0.007	26	4	55	13	31	2.65	19.5
Unit A'	0.029	.0005	43	1	77	13	36	2.62	20.5
Unit B	0.017	.0006	42	2	86	-	-	2.55	20.0

Table 1. Physical properties of the river embankment soils.

Soil unit	θr	θsat	α_{VG}	n_{VG}	k_{sat}	φ'	c'
-	m³/m³	m³/m³	kPa	-	m/sec	°	kPa
Unit A	0.004	0.397	11.5	1.304	6.2E-07	30.6	0.0
Unit A'	0.001	0.319	39.2	1.284	4.6E-07	33.4	0.0
Unit B	0.000	0.424	83.3	1.142	3.3E-09	24.9	0.0
Unit C	-	-	-	-	3.1E-07	30.0	0.0
Unit D	-	-	-	-	1.4E-09	22.5	0.0
Unit E	0.005	0.366	60.9	1.307	9.0E-08	24.9	0.0

Table 2. Soil retention, hydraulic and mechanical parameters used in numerical model.

Borehole	Probe	Installation depth (m b.g.l.)	Measurement
MPC1	GS3	2.4	Water content
	MPS-6	3.1	Suction
	GS3	4.5	Water content
	MPS-6	4.6	Suction
SPC1	MPS-6	7.0	Suction
SPC2	GS3	7.1	Water content
TC1	T8	4.7	Pore pressure
TC2	T8	8.0	Pore pressure
MPC2	MPS-6	1.2	Suction
	SM150T	1.5	Water content
MPC3	GS3	1.4	Water content
	MPS-6	6.2	Suction
	GS3	6.4	Water content
SPC3	SM150T	7.1	Water content
MPB1	GS3	0.7	Water content
	MPS-6	0.9	Suction
MPB2	GS3	2.2	Water content
	MPS-6	2.7	Suction
TB1	T8	4.9	Pore pressure
SPB1	MPS-6	1.2	Suction

Table 3. Monitoring system details.